

**Using Markov Chain Monte Carlo Inversion to Characterize the Rheology of
the Early Hadean Upper Mantle**

Brianna Fernandez

Advisor: Prof. Jun Korenaga

Second Reader: Prof. Shun-ichiro Karato

9 May 2023

A Senior Essay presented to the faculty of the Department of Earth and Planetary Sciences, Yale University, in partial fulfillment of the Bachelor's Degree.

In presenting this essay in partial fulfillment of the Bachelor's Degree from the Department of Earth and Planetary Sciences, Yale University, I agree that the department may make copies or post it on the departmental website so that others may better understand the undergraduate research of the department. I further agree that extensive copying of this thesis is allowable only for scholarly purposes. It is understood, however, that any copying or publication of this thesis for commercial purposes or financial gain is not allowed without my written consent.

Brianna Fernandez, 9 May 2023

Contents

Abstract	2
1 Introduction	3
2 Theoretical Formulation	5
2.1 Flow Law	5
2.2 Statistical Model for Experimental Data	6
2.3 Markov Chain Monte Carlo with Gibbs Sampling	8
3 Deformation Data	12
4 Results	16
4.1 Inversion with Individual Experimental Runs	16
4.1.1 High-Stress Dry Dislocation-Only Creep	17
4.1.2 High-Stress Dry Dislocation-Only Creep for a Combined Data Set.	19
4.2 Composite Inversion with Combined Data Sets	21
4.2.1 Composite Dry Dislocation and Diffusion Creep for All Stresses	21
5 Discussion	25
5.1 Comparison with <i>Bystricky et al. (2016)</i>	25
5.2 Covariance	27
5.2 Implications for the Early Hadean Upper Mantle	28
6 Conclusion	30
Acknowledgments	31
References	32
Appendix	34

Abstract

The early Hadean upper mantle was likely orthopyroxene-dominated, and investigating the rheological properties of this mineral is significant for an understanding of the dynamics of the early mantle. In this work, we apply the Markov chain Monte Carlo (MCMC) inversion method of *Mullet et al. (2015)* to published laboratory data on the deformation of orthoenstatite aggregates from *Bystricky et al. (2016)* with the aim of establishing experimental bounds on early Hadean upper mantle rheology. We focus on the two creep tests conducted in the orthoenstatite stability field, first performing reanalyses of individual and combined data sets with stresses above 200 MPa for dry dislocation creep deformation mechanisms. We then perform simultaneous inversions for the flow-law parameters of orthoenstatite in both dry diffusion creep and dry dislocation creep regimes, showing that composite rheology inversion provides a better fit to the data. Composite inversion yields a median activation energy for dislocation creep of $Q_1 = 637$ kJ/mol, a median activation energy for diffusion creep of $Q_2 = 352$ kJ/mol, and a median stress exponent of $n = 2.61$ in the dislocation creep regime. Our flow-law parameters demonstrate a higher activation energy and a smaller stress exponent for orthoenstatite when compared to the parameters reported by *Bystricky et al. (2016)*. We illustrate the importance of considering both dislocation and diffusion deformation mechanisms when constraining flow-law parameters and emphasize the need for more experimental effort in understanding rheological properties of the Hadean upper mantle, particularly for lower-stress conditions and wet deformation mechanisms.

1. Introduction

While the present-day Earth is distinct for its ability to sustain life, Earth in the early Hadean had a significantly different temperament. In the first few hundred million years after the solidification of a magma ocean, Earth was an inhospitable world with extreme surface temperatures originating from a thick, Venus-like atmosphere containing levels of carbon dioxide hundreds of thousands of times greater than that of the modern Earth. Geological records suggest that during the Hadean, Earth's surface had dramatically transformed from this harsh environment to a stable, habitable one similar in climate and temperature to those of the modern Earth, but how such transformation was achieved has been a mystery. A recent theory suggests that a mantle dominated by magnesium-rich pyroxene may have been the key (Miyazaki & Korenaga, 2022). After the early Earth's magma oceans underwent solidification, the resulting hydrated mantle convected rapidly, working in conjunction with magnesium-rich pyroxenites and iron-rich silicates to sequester atmospheric carbon at accelerated rates. This process would occur ten times faster with a pyroxene-dominated mantle than with one of a modern composition, matching the rates indicated by ancient geologic records (Miyazaki & Korenaga, 2022).

As a result of mechanical mixing and chemical re-equilibration in mantle convection, Earth's upper mantle is now largely composed of olivine. Due to its large volume fraction (~60%) of Earth's upper mantle, olivine regulates the rheology of the upper mantle (Karato, 2008). Consequently, the mineral and its rheological properties have been comprehensively researched, resulting in the continual development of flow laws, which describe olivine's strain rate as a function of stress and other relevant state variables (e.g., Korenaga & Karato, 2008; Mullet et al., 2015). The rheology of mantle materials is integral to the determination of its

behavior under stress at different temperature and pressure conditions. As the early Hadean upper mantle was likely orthopyroxene-dominated, investigating this mineral's rheological properties is significant for an understanding of early mantle dynamics. By finding the rheological parameters of orthopyroxene, one could characterize the early mantle based on laboratory-derived deformation data. My essay will explore this idea, searching for a set of flow-law parameters that explain experimentally measured strain rates of orthoenstatite, a magnesium-rich orthopyroxene mineral.

2. Theoretical Formulation

2.1 Flow Law

Our understanding of orthopyroxene rheology comes from decades of experiments that aimed to characterize it in diffusion and dislocation creep regimes (see, e.g., Raleigh et al., 1971; Ross and Nielsen, 1978; Dehghan et al., 1981, 1982; Hitchings et al., 1989; Mackwell et al., 1991; Lawlis, 1998; Ji et al, 2001). Dislocation creep is a deformation mechanism by which plastic strain is accommodated by the motion of dislocations through the crystal lattice, and is significant at higher stresses. Diffusion creep, which predominates at lower stresses, is a deformation mechanism by which plastic strain is accommodated by the diffusion of atoms through the crystal lattice (Karato, 2008). The point at which one deformation mechanism dominates depends on temperature, pressure, grain size, and water content (e.g., Korenaga & Karato, 2008).

Our study focuses on diffusion and dislocation creep in water-poor, or “dry,” conditions in our efforts to constrain the rheology of orthopyroxene, assuming the following flow laws:

$$\dot{\varepsilon}_{dis, dry} = A_1 \sigma^n \exp\left(-\frac{Q_1}{RT}\right) \quad (1)$$

$$\dot{\varepsilon}_{diff, dry} = A_2 d \sigma \exp\left(-\frac{Q_2}{RT}\right) \quad (2)$$

Here, $\dot{\varepsilon}$ is strain rate in s^{-1} , its subscripts specifying either dislocation creep (‘dis’) or diffusion creep (‘diff’) mechanisms at dry conditions. A_i is a scaling constant, σ is stress in MPa, Q_i is activation enthalpy in $Jmol^{-1}$, n is a stress exponent, d is average grain size in microns, R is the universal gas constant, and T is absolute temperature. Both A_i and Q_i change according to the deformation mechanism—dry diffusion creep or dry dislocation creep. We do not consider grain size dependence or activation volumes in our flow laws.

Diffusion creep and dislocation creep can take place in parallel, being dominant at different stress conditions, so the total strain rate of a deformed orthopyroxene sample can be expressed as a sum of the two:

$$\dot{\varepsilon}_{comp} = \sum_i \dot{\varepsilon}_i = \dot{\varepsilon}_{dis} + \dot{\varepsilon}_{diff}, \quad (3)$$

where $\dot{\varepsilon}_{comp}$ is a composite strain rate from the combination of both deformation mechanisms, the subscript i indicating either dislocation (1) or diffusion (2) creep. Typical deformation experiments are conducted at stresses close to the point at which the transition between dominant deformation mechanisms occurs, motivating the separation of each mechanism's contributions to strain rate via global inversion. As of the writing of this essay, there has been no instance of simultaneous inversion for the flow-law parameters of enstatite.

2.2 Statistical Model for Experimental Data

We aim to determine flow-law parameters according to the assumed flow laws, accounting for strain rate measurements of enstatite given their experimental uncertainties. The statistical model used for measured strain rate data is given by the following from *Korenaga & Karato (2008)*:

$$\dot{\varepsilon}_{obs}^{j_m} = \left(\sum_i \dot{\varepsilon}_i(\{q_k\}; \{s_l^j\}) \right) \exp(X^{j_m}). \quad (4)$$

Here, $\dot{\varepsilon}_{obs}^{j_m}$ represents the observed strain rate for the j_m -th experiment in the m -th run, $\{q_k\}$ is a set of flow-law parameters such as A_i and Q_i , $\{s_l^j\}$ is a set of relevant state variables for j -th experiment such as temperature T^j and pressure P^j , and $\dot{\varepsilon}_i(\{q_k\}; \{s_l^j\})$ is the corresponding

theoretical prediction of the strain rate (Mullet et al., 2015). X is a random variable, meant to account for the variabilities not modeled by the flow laws (1) and (2), such as grain size distribution and oxygen fugacity (Korenaga & Karato, 2008). Systemic bias in an experimental run, represented by $\exp(X)$, relies on the assumption that some unquantified parameters remain constant throughout the run (Korenaga & Karato, 2008). In this assumption, the random variable X , or the inter-run bias, is constant for each individual run but may change between them. In general, high-stress dry runs—runs for which dislocation creep is the dominant deformation mechanism—demonstrate relatively low inter-run bias, and lower-stress dry runs, or those in the diffusion creep regime, demonstrate systematic differences depending on grain size (Korenaga & Karato, 2008).

To evaluate the effectiveness of flow-law parameters, we use the following cost function developed by *Mullet et al.* (2015) to measure the misfit between observed and predicted strain rates:

$$\chi^2(\{q_k\}, \{\chi_m\}) = \sum_{m=1}^M \sum_{j_m=1}^{N_m} \frac{(\log \dot{\epsilon}_{obs}^{j_m} - \log \dot{\epsilon}(\{q_k\}; s_l^{j_m})) - X_m)^2}{rvar(\dot{\epsilon}_m^{j_m})}. \quad (5)$$

This is a modification of the cost function originally proposed by *Korenaga & Karato* (2008) and considers the relative variance of strain rate and the uncertainty of other state variables. Here, M represents the number of experimental runs while N_m represents the number of experiments in the m -th run. Because strain rates are often provided as relative error and compared logarithmically, the denominator term $rvar\{\dot{\epsilon}_j\}$, which denotes a relative variance from the measured strain rate error, is defined as:

$$rvar\{\dot{\epsilon}_j\} = \frac{var\{\dot{\epsilon}_j\}}{(\dot{\epsilon}_{obs}^j)^2}. \quad (6)$$

(Korenaga & Karato, 2008).

The cost function is valuable in the estimation of both flow-law parameters and inter-run biases. By propagating state variable uncertainty into flow-law parameters via the random perturbations of experimental data, we create a model that minimizes parameter bias with a Bayesian approach (Mullet et al., 2015).

2.3 Markov Chain Monte Carlo with Gibbs Sampling

Since deformation experiments are conducted over hours rather than geological timescales, their derived strain rates are about ten orders of magnitude faster than their geologic analogs. These accelerated strain rates are achieved by increasing stresses while decreasing grain sizes. For example, stresses in the mantle are on the order of 0.1 MPa while many deformation experiments use stresses on the order of ~100 MPa. Extrapolating rheologies from experiments bound by these constraints would be subject to many nontrivial experimental uncertainties (Korenaga & Karato, 2008).

The estimation of flow-law parameters from deformation data is a complex nonlinear inverse problem, which may be best analyzed by Markov chain Monte Carlo (MCMC) inversion (Korenaga & Karato, 2008). MCMC methods are a class of algorithms which use random sampling based on Markov chains to approximate probability distributions given a number of iterations, estimating model parameters from data in a Bayesian framework. They are called "inversion methods" because they estimate the parameters by inverting the conditional probability of the data given the parameters (the "likelihood"), which is proportional to the posterior probability of the parameters given the data. This project employs MCMC inversion

methods according to the steps described by *Mullet et al.* (2015), which was modified from *Korenaga & Karato* (2008). This MCMC algorithm may be summarized as the following steps:

1. *Initialization.* The algorithm begins by drawing a quantity of random numbers to be estimated from $[0,1]$ and setting the iteration counter to 0.

2. *Data Randomization.* This step stipulates that all experimental data should be randomized within their uncertainties if the iteration counter is a multiple of an established integer. This mitigates bias via error propagation from the cost function, as described by *Mullet et al.* (2015). If the iteration counter falls outside of the multiples of the specified integer, the data from the last iteration is used.

3. *Random Scan.* This step relies on the conditional likelihood, which is created after the random selection of a model parameter. Random numbers are drawn from the interval of a priori upper and lower bounds, and their likelihood values are then calculated from the cost function. The absence of a priori bounds for scaling constants requires that they are considered separately from other flow-law parameters for the efficient implementation of an MCMC algorithm, as they vary over orders of magnitude due to their strong coupling with other parameters. *Mullet et al.* (2015) derive scaling constants through the application of a conjugate gradient search, selecting the smallest value of the cost function from multiple initial guesses. If enough random numbers are drawn from the interval of a priori bounds, rejection sampling can yield the approximation of the conditional likelihood, from which the highest likelihood is saved as L_{max} .

4. *Gibbs Sampling.* Gibbs sampling is a type of MCMC algorithm that is used to estimate the posterior distribution of model parameters. It iteratively samples values from the conditional distribution of each parameter given the current values of all the other parameters until the desired number of samples is obtained. At each iteration, the value of one parameter is updated

while keeping all other parameters fixed based on its conditional distribution. This process continues until convergence, at which point the sampled parameter values approximate the posterior distribution of the model parameters. As Gibbs sampling does not require tuning, it can efficiently explore high-dimensional parameter spaces with complex dependencies between parameters (Korenaga & Karato, 2008). Additionally, it is highly efficient, as demonstrated by the distribution of χ^2/N (χ^2 normalized by N , the number of data) shown in the Results section. This distribution suggests that the Gibbs sampling algorithm was able to efficiently explore the parameter space and efficiently generate a large quantity of samples, resulting in a reliable estimate of the posterior distribution of the model parameters without the need for extensive tuning or computation.

5. *Model Update.* After those steps, the model is updated with the new calculated flow law parameters, the iteration counter increases by one, and the process repeats from step 2 until the maximum number of iterations is reached.

This method of random-scan Gibbs sampling produces highly correlated ensembles of saved models, as only one parameter is perturbed at each iteration, so each ensemble must be resampled at long intervals for the models to be statistically independent. An autocorrelation function determines the interval by which the ensemble is resampled, providing an ensemble from which the mean and covariance of model parameters can be easily calculated, and the convergence of the sampling is verified by comparing the results of parallel runs sampled with different initial models. When the distributions are consistent across all runs, it is an indication that they have reached convergence and that the parameter space has been thoroughly explored (Mullet et al., 2015).

In this work, we apply this approach to published data on the deformation of enstatite aggregates with the aim of establishing experimental bounds on early Hadean upper mantle rheology.

3. Deformation Data

As the primary constraints on the rheological parameters of minerals come from laboratory experiments, we apply the MCMC inversion method outlined above to orthopyroxene deformation data from *Bystricky et al. (2016)*. *Bystricky et al. (2016)* performed high-temperature deformation experiments on enstatite aggregates, from which they constrained creep flow laws. Several previous studies analyzed the deformation of single enstatite crystals (e.g., *Dehghan et al., 1981, 1982*; *Schloessin & Ranalli, 1988*; *Hitchings et al., 1989*; *Mackwell et al., 1991*; *Ohuchi et al., 2011*; *Raterron et al., 2016*) but fewer analyzed crystal aggregates. It is important to study crystal aggregates, as the behavior of aggregates is different from that of single crystals and provides a better analog for their natural contexts in the Earth's mantle.

Mackwell et al. (1991) performed experiments on single orthopyroxene crystals to investigate their deformation behavior under high temperatures. The experiments were conducted under room pressure conditions and favored slip on the easiest dislocation slip systems, and they demonstrated that, unlike olivine, the deformation behavior of enstatite does not have a dependence on oxygen fugacity. The results also showed that the strengths of enstatite are significantly higher than for the easier slip systems in olivine under comparable conditions.

Previous work on natural orthopyroxene aggregates under dry conditions includes that conducted by *Raleigh et al. (1971)*, which demonstrated that deformation at temperatures greater than 1000°C and confining pressures of 1–2 GPa primarily involves the (100)[001] slip system and reported measurements of a stress exponent of $n = 2.4$ and an activation energy of $Q = 290$ kJ/mol. However, the orthopyroxenite samples used in their deformation experiments were not pre-dried before deformation, resulting in non-zero water fugacities, which produced flow-law parameters similar to those found in wet experiments. This combined with differing experimental

conditions and uncertainties in their stress measurements resulting from friction in their apparatus makes difficult comparisons to data from *Bystricky et al. (2016)* and motivates further study of enstatite crystal aggregates.

Bystricky et al. (2016) performed fifty triaxial compressive creep tests on four synthetic enstatite samples in a Paterson gas-medium apparatus at constant load. The applied load was measured with an internal load cell which yielded differential stresses accurate to ± 2 MPa and determined sample strains from the displacement of a piston measured using a linear variable differential transducer outside of the pressure vessel. The deformation experiments entailed constant-load stepping tests at temperatures from 1473 K to 1573 K and confining pressures of either 300 MPa or 450 MPa. *Bystricky et al. (2016)* chose applied loads to ensure that the achieved differential stresses did not significantly exceed the confining pressure, and the applied loads were held constant at each deformation step until an approximate steady-state creep rate was achieved. After reaching experimental pressure and temperature conditions, the samples equilibrated for at least two hours before deforming, enabling them to completely transform to either protoenstatite (300 MPa) or orthoenstatite (450 MPa).

Table 1. Experimental Conditions for Creep of Enstatite Aggregates

Experiment	Hot Press			Deformation				
	P_c (MPa)	T (K)	t (h)	P_c (MPa)	T Range (K)	σ Range (MPa)	ϵ_{tot} (%)	Grain Size (μm)
PI-512	450	285	12	450	1473-1548	170-430	23	3-10
PI-539	450	281	8	450	1473-1523	111-460	21	3-10

After *Bystricky et al. (2016)*. P_c is the confining pressure, T is the temperature of the hot press, and t is its duration. In describing deformation data, “ T Range” refers to the range of temperatures achieved during deformation, as “ σ Range” refers to the range of stresses achieved, and ϵ_{tot} is the total strain.

We focus on the two creep tests conducted in the orthoensatite stability field, or those performed at a confining pressure of $P_c = 450$. The hot-pressing and deformation conditions for these two tests, experiments PI-512 and PI-539, are detailed in Table 1. The pressure and temperature conditions and creep data derived from the creep tests are listed in Table 2 in the appendix. As seen in Figure 1, these two runs were conducted under similar experimental conditions.

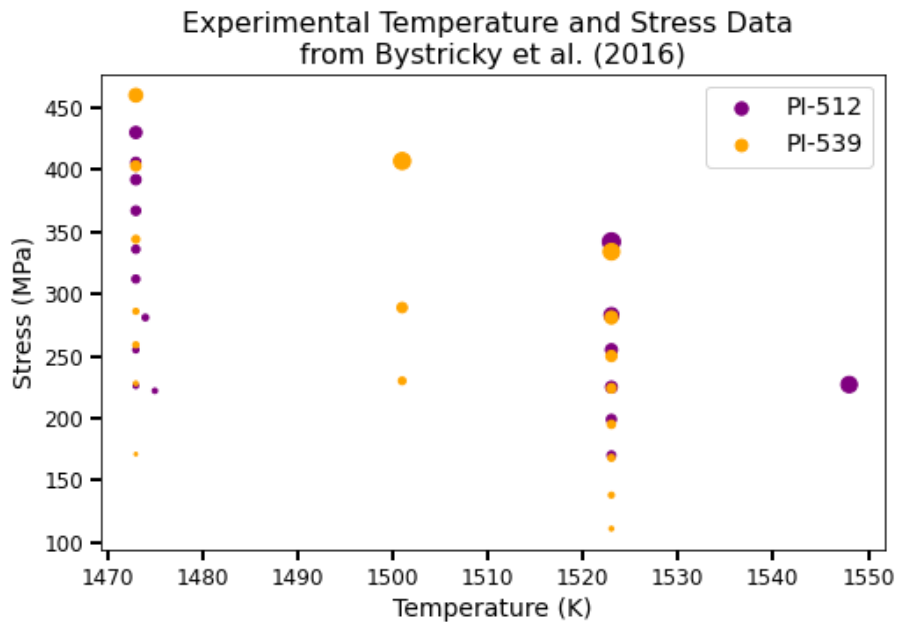


Figure 1. A visualization of the experimental temperature and stress data from two runs performed by *Bystricky et al. (2016)*. The sizes of the points depicting the data vary depending on strain rate and range from $1.2 \times 10^{-6} \text{ s}^{-1}$ to $4.6 \times 10^{-6} \text{ s}^{-1}$. A full table of the experimental data is provided in the appendix.

Bystricky et al. (2016) calculated strain rates and flow stresses from the displacement and load data, the relationship between which is shown by Figure 2 for experiments PI-512 and PI-539. The strain rate versus differential stress data indicate a power-law relationship at stresses above 200 MPa, which suggests that they can be fit to the flow law for dislocation creep described by Equation (1), as the effects from diffusion creep are minimal. The stress exponents

obtained from fits to the data at a constant temperature and stresses higher than 200 MPa ranged between $n = 2.8$ and 3.1 .

To determine the activation energy and pre-exponential term for creep of orthoenstatite, they performed global nonlinear least squares regressions on data sets at stresses above a fixed threshold with a fixed $n = 3.0$ for all regressions. The regression for data measured at a confining pressure of 450 MPa and stresses greater than 200 MPa yielded an activation energy $Q = 600 \pm 21$ kJ/mol and a pre-exponential term $A = 108.63 \pm 0.73$ MPa³ s⁻¹. When using data for a broader range of stresses—those above 150 MPa—they obtained activation energies of $Q = 621 \pm 22$ kJ/mol, and when using data for stresses above 250 MPa, they obtained activation energies of 583 ± 23 kJ/mol.

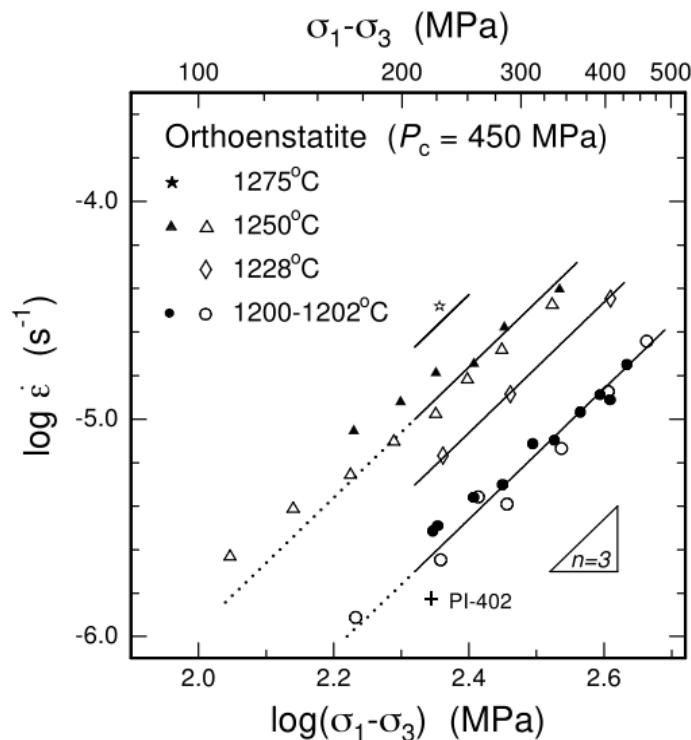


Figure 2. Reproduced from *Bystricky et al.* (2016). Plot of log strain rate versus log stress for creep data from experiments PI-512 and PI-539, represented by solid and open symbols, respectively. These data result from the deformation of dry orthoenstatite in the orthoenstatite field ($P_c = 450$) at stresses higher than 200 MPa and temperatures of 1473, 1501, 1523, and 1548 K (listed on the plot in Celsius), represented by solid lines that are extended by dotted lines ones to depict the flow law at lower stress conditions.

4. Results

In this section, we report results from our MCMC analysis of experiments PI-512 and PI-539 from *Bystricky et al. (2016)*. We begin with a reanalysis of the data from each individual experiment for stresses above 200 MPa before reporting our results generated by inverting the data derived from experiments PI-512 and PI-539 combined. We first reanalyzed this data at stresses above 200 MPa for only dislocation creep deformation mechanisms, similar to our approach used for the individual runs, before expanding our approach to all stresses to evaluate both diffusion creep and dislocation creep mechanisms.

In implementing our MCMC inversion method, we set the maximum number of MCMC iterations as 10^5 , with an iteration interval of 10 for data randomization, 75 trials in Gibbs sampling, and 10 initial guesses in the conjugate gradient search. An ensemble was resampled with an interval of 100, making the size of a resampled ensemble 10^3 for each run.

We note that, for much of the data, the normalized cost function χ^2/N is greater than 1, implying that the average misfit between the data and model prediction is larger than the average prescribed experimental uncertainty. This indicates that some of the experimental uncertainties may have been underestimated or that the assumed flow law is inadequate. More experimental data are necessary to investigate this issue.

4.1 Inversion with Individual Experimental Runs

In this section, we report results from our MCMC analysis of individual experiments PI-512 and PI-539 from *Bystricky et al. (2016)*. Because we analyzed these experiments individually, we do not need to account for inter-run bias, meaning $X = 0$. The a priori range for

these inversions' activation energies (in kJ/mol) was set at [0, 800], and the a priori range was set as [1.0, 6.0] for the stress exponent.

4.1.1 High-Stress Dry Dislocation-Only Creep

In our consideration of individual experimental data with stresses over 200 MPa, we neglect diffusion creep, as these higher stresses can be considered to be out of the diffusion creep regime. Figure 2 illustrates the MCMC inversion results for each of the deformation experiments in the orthoenstatite field, demonstrating that the predicted strain rates match those measured by *Bystricky et al.* (2016).

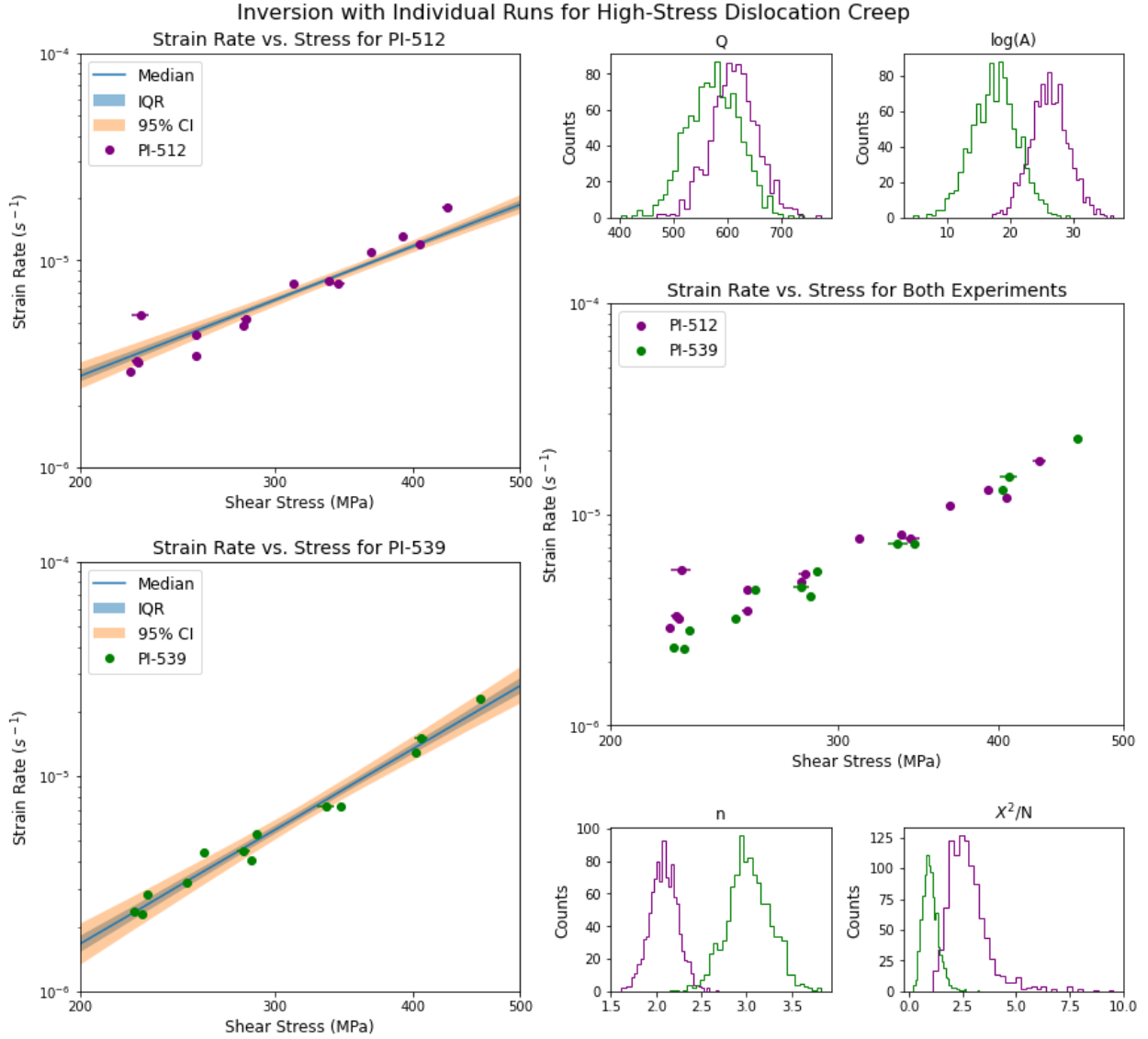


Figure 3. Data and flow law prediction are shown in the leftmost plots for the data derived by experiments PI-512 (top) and PI-539 (bottom). Blue and orange shadings denote 50% and 95% confidence intervals (CI), respectively. The plot of log strain rate versus log stress to the right depicts the data plotted together, with PI-512 represented in purple and PI-539 represented in green. Also shown are the distributions of the activation energy (Q), scaling constant ($\log(A)$), stress exponent (n), and normalized χ^2 . Purple and green histograms correspond to inversion with PI-512 and PI-539, respectively.

The figure also includes histograms illustrating the flow-law parameters constrained by the MCMC inversion. Our approach found a median activation energy $Q = 613$ kJ/mol and a median stress exponent $n = 2.08$ for PI-512 and found a median activation energy $Q = 575$ kJ/mol and median stress exponent $n = 3.00$ for PI-539. The pre-exponential term A for PI-512

and PI-539 was $A = 10^{26.21} \text{ MPa}^{-3}\text{s}^{-1}$ and $A = 10^{17.55} \text{ MPa}^{-3}\text{s}^{-1}$, respectively. While these individual runs produced similar activation energy parameters, their stress exponents varied considerably. As the stress exponent parameter is related to strain rate via a power law relationship, a higher n value indicates a greater sensitivity of the deformation rate to changes in stress, whereas a lower value indicates a weaker sensitivity. A small change from $n \approx 2$ to $n \approx 3$, as reflected by the parameters found between experiments, would suggest an increase in strain rate by over three orders of magnitude when extrapolating from experimental conditions ($\sim 100 \text{ MPa}$) to mantle conditions ($\sim 0.1 \text{ MPa}$).

4.1.2 High-Stress Dry Dislocation-Only Creep for a Combined Data Set

Simultaneous inversion of both data sets for only the dislocation creep regime enables better constraints on flow law parameterization, as more data points induce a better model fit. Figure 4 depicts the MCMC inversion results for the combined experimental runs. The MCMC inversion for this data set produced flow-law parameters $Q = 601 \text{ kJ/mol}$, $A = 10^{23.83} \text{ MPa}^{-3}\text{s}^{-1}$, and $n = 2.34$. The stress exponent constrained by this inversion is remarkably smaller than that reported by *Bystricky et al.* (2016) ($n = 3.0$), suggesting weaker sensitivity of the deformation rate to stress changes and orders of magnitude difference in mantle strain rate than predicted by *Bystricky et al.* (2016). This disparity in n value emphasizes the effect that different methods induce on parameter constraints, particularly on the stress exponent.

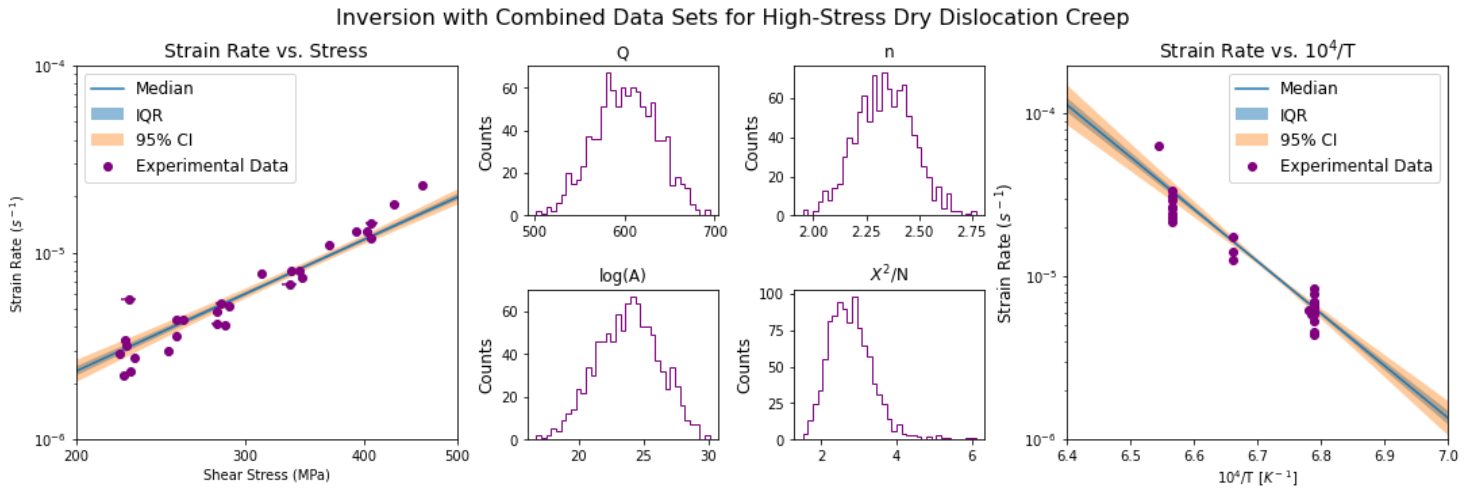


Figure 4. Data and flow law prediction similar to Figure 3 but for inversion with a single data set from data derived by experiments PI-512 and PI-539. Also included is a plot of inverse temperature versus strain rate (right).

Table 2 illustrates the flow-law parameters found for each of the described inversions, providing a compilation of the relevant results generated from inversions solely in the dry dislocation creep regime.

Table 2. Inversion Results for Dry Dislocation-Only Creep

Inversion	Experiment	Q (kJ/mol)	$\log_{10}(A)$ ($\text{MPa}^{-3}\text{s}^{-1}$)	n
High-Stress Dry Dislocation-Only Creep	PI-512	613.11	26.210	2.0797
	PI-539	574.56	17.552	3.0136
Combined High-Stress Dry Dislocation-Only Creep	PI-512 and PI-539	601.34	23.830	2.3388

However, the effect of diffusion creep on flow-law parameters, even at high stresses, is not negligible. Estimated activation energy uncertainties are likely affected by contributions from diffusion creep flow laws, especially when the experimental data lie near the transition zone

between flow law deformation mechanisms, as the data from *Bystricky et al. (2016)* do (Korenaga & Karato, 2008). As noted by *Mullet et al. (2015)*, parameters from single-run inversions are better considered as apparent values than those constrained by more reliable estimates from composite inversions, rendering these findings better as approximations.

4.2 Composite Rheology Inversion with Combined Data Sets

In this section, we combined experimental runs before inverting for flow-law parameters rather than running the inversions with individual data sets and making sequential extrapolations. However, for these inversions we combined flow laws, making more stable inversions and allowing for the estimation of activation energies of different creep mechanisms separately while automatically taking care of the interrelation of parameter uncertainties. This reduces misleading results produced by the methods described above which ignore seemingly irrelevant creep regimes, particularly when the majority of data lie near the transition between regimes (Korenaga & Karato, 2008).

We report results from our MCMC analysis of combined experiments PI-512 and PI-539, necessitating that we account for inter-run bias, X . The a priori range for activation energies (in kJ/mol) was set at $[0, 1000]$, and the a priori range was set as $[1.0, 5.0]$ for the stress exponents. This inversion of parallel deformation mechanisms also considers grain size, which we assumed to be constant at 10 microns.

4.2.1 Dry Dislocation and Diffusion Creep for All Stresses

The simple combination of diffusion creep and dislocation creep can better explain experimental data, as uncertainties from both deformation mechanisms cannot plague derived

parameters from one flow law or another. This combination encourages a wholesale approach to the constraint of flow-law parameters and allows for the consideration of more parameters which affect deformation. To obtain a complete flow law that encompasses both diffusion and dislocation creep components, as illustrated by Equation (3), more measurements need to be taken in unambiguously diffusion and dislocation creep fields (Bystricky et al., 2016).

Figure 5 shows the inversion results for both deformation regimes after the combination of experimental data. With a median activation energy for dislocation creep of $Q_1 = 637$ kJ/mol and a median activation energy for diffusion creep of $Q_2 = 352$ kJ/mol, demonstrating a higher activation energy for dislocation creep than the other inversions, likely because it is not diluted by uncertainties from diffusion creep. The median pre-exponential term for the dislocation creep regime was $A_1 = 10^{24.84}$ MPa⁻³s⁻¹ and $A_2 = 10^{9.21}$ MPa⁻³s⁻¹ for the diffusion creep regime. For dislocation creep, we found $n = 2.61$.

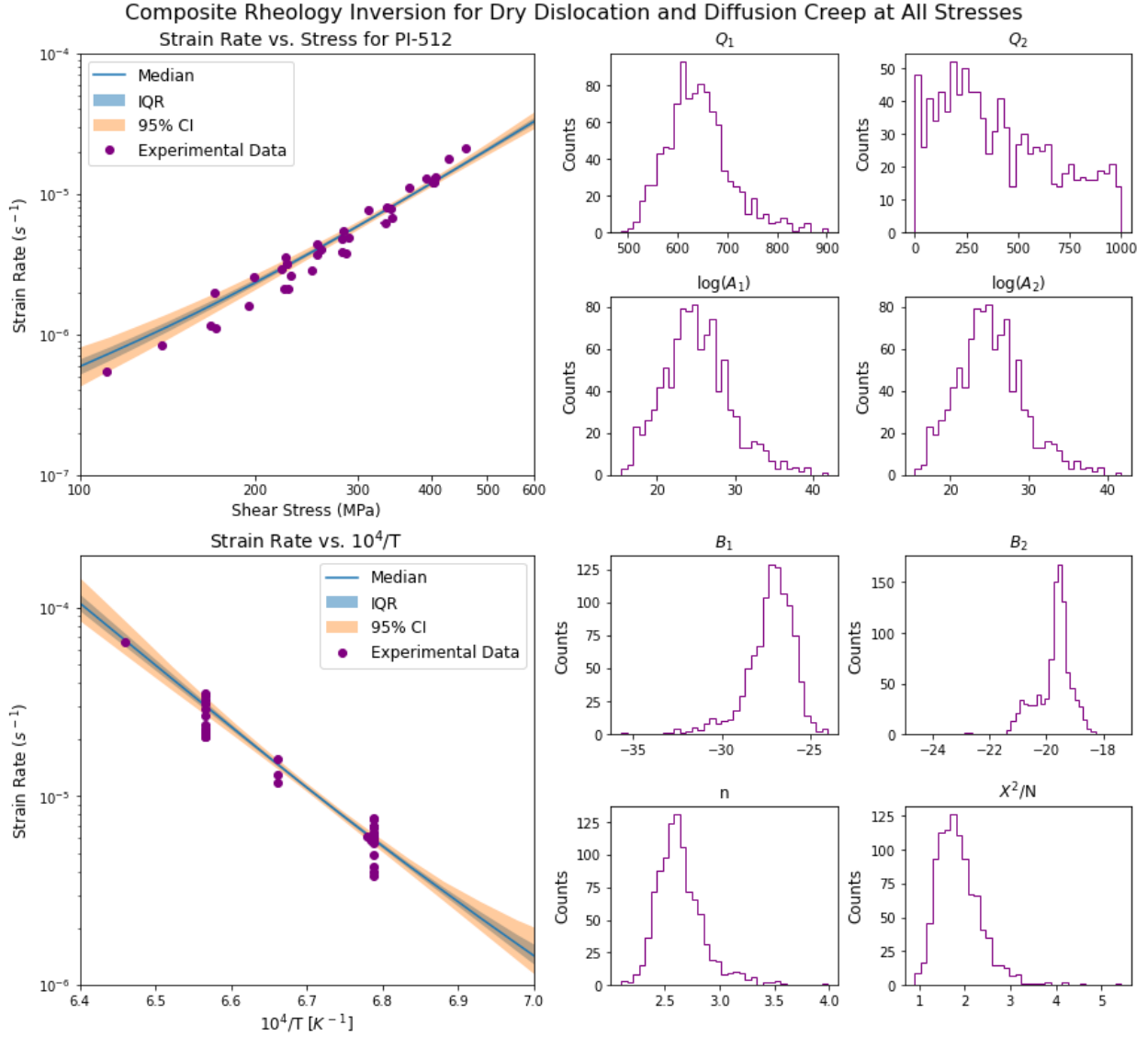


Figure 5. Data and flow law prediction are shown in the top left plot for composite rheology inversion of the combined data set with 50% and 95% confidence intervals represented by blue and orange shadings, respectively. The bottom left plot depicts inverse temperature versus strain rate, and the histograms to the right illustrate distributions of the activation energy (Q_i), scaling constant ($\log(A_i)$), Q -normalized scaling constant (B_i), stress exponent (n), and normalized χ^2 for dislocation (1) and diffusion (2) creep.

The inversion results with composite rheology provide a better fit to the data overall. This can be seen on the plot depicting shear stress versus strain rate in Figure 5, as the experimental data conforms nicely to the predicted curve due to the incorporation of low-stress values and the utilization of diffusion creep flow laws. Importantly, this better fit shows a slightly higher activation energy than previously modeled by our other inversions or *Bystricky et al.* (2016). A

higher activation energy Q in a creep mechanism indicates that the material requires more energy to initiate and propagate dislocations, which are the primary mechanism of deformation. Since the material is more resistant to deformation at a given temperature, higher temperatures or higher stresses are needed to induce creep. Furthermore, higher activation energy also suggests that the material is more stable at lower temperatures, as it takes more energy to cause atomic rearrangements necessary for deformation.

Effects from diffusion creep, while poorly constrained, are still quite present in the data. A full understanding of a material's rheology cannot be obtained through examination of data using only one deformation regime's flow law. Even high-stress data cannot be fit in the dislocation creep regime alone, as even at higher stresses, the data are influenced by other deformation mechanisms.

5. Discussion

5.1 Comparison with Bystricky et al. (2016)

Comparing composite flow laws in terms of the scaling constants is not very informative, as a small change in activation energies can result in a large variation in the scaling constants, so we do not consider A_i in our data comparison. *Mullet et al. (2015)* and *Korenaga & Karato (2008)* use the following conversion to reduce the variation of this scaling constant:

$$B_i = \log_{10} \left(A_i \exp \left(\frac{-Q_i}{RT_{ref}} \right) \right), \quad (7)$$

for which we set T_{ref} as 1473 K. For example, the scaling constants A_i generated by composite rheology inversion might be better embodied by the values by normalized scaling constant $B_1 = -27.08$ using parameters generated from dislocation creep and $B_2 = -19.62$ from those in the diffusion creep regime.

We compare our resulting flow-law parameters from composite inversion with the published parameters from *Bystricky et al. (2016)*. They determined that the orthoenstatite data fall mainly in the dislocation creep field but acknowledge that they show contributions from diffusion creep at lower stresses. However, it should be noted that the data from *Bystricky et al. (2016)* listed in the table is for stresses greater than 200 MPa and was only considered according to the dislocation creep flow law. Though they acknowledge potential effects from diffusion creep, their flow-law parameters do not, making it difficult to compare our composite data to theirs.

Table 3. Comparison of Composite Inversion Results with Parameters from *Bystricky et al. (2016)*

Parameter	<i>Bystricky et al. (2016)</i>	This Study
n	3.0	2.6110 ± 0.216
Q_1	600 ± 21	636.76 ± 65.115
Q_2	-	351.85 ± 273.62
$\log(A_1)$	8.63 ± 0.73	24.834 ± 4.2870
$\log(A_2)$	-	9.2059 ± 21.767
B_1	-	-27.075 ± 1.3391
B_2	-	-19.619 ± 1.9531

Broadly, our more tightly constrained flow-law parameters indicate a higher activation energy and a smaller stress exponent. Comparing our parameters produced by combined dislocation creep inversion shows an even smaller stress exponent of $n = 2.34$, though the resulting activation energy is within their determined value at $Q = 601$ kJ/mol. This underscores the importance of considering both deformation mechanisms when constraining flow-law parameters, particularly when the data studied are from experiments conducted at stresses close to the point at which the transition between dominant deformation mechanisms occurs. Our understanding of rheology can vary drastically depending on their derived flow-law parameters, as the differences between our stress exponents and those found by *Bystricky et al. (2016)* imply strain rates that differ, when extrapolated to mantle conditions, by orders of magnitude, emphasizing the diligence with which researchers must consider their parameters and the methods they use to constrain them.

5.2 Covariance

As the uncertainties of different flow law parameters are not independent, reporting only the mean and standard deviation of flow law parameters from composite inversions is not sufficient for conducting sensitivity tests. Flow law parameters are often correlated with one other, so perturbing one parameter can affect the uncertainty of others. Constructing a correlation coefficient matrix based on the MCMC ensemble can account for this correlation, from which the direction and magnitude of parameter perturbations can be determined. The parameter correlation coefficient matrix is a normalized covariance matrix and may be calculated by multiplying the standard deviations of each flow-law parameter and dividing the covariance between them by that value (Mullet et al., 2015). Table 4 depicts correlation coefficients for the flow-law parameters derived by composite MCMC inversion and include B_i for scaling constant A_i , considering the characteristic high variability of the latter.

Table 4. Correlation Coefficients for Flow-Law Parameters

	n	Q_1	Q_2	B_1	B_2
n	1.000000	0.797445	-0.365788	-0.998477	0.256498
Q_1	0.797445	1.000000	-0.660569	-0.820416	0.269292
Q_2	-0.365788	-0.660569	1.000000	0.391648	-0.334016
B_1	-0.998477	-0.820416	0.391648	1.000000	-0.268251
B_2	0.256498	0.269292	-0.334016	-0.268251	1.000000

As indicated by the table, Q_I and n are strongly positively correlated, the only strong positive correlation observed, suggesting that these two parameters are not well resolved. The strong negative correlation between B_I and Q_I is surprising, because the conversion from A_I to B_I is supposed to reduce such correlation. B_I also strongly correlates with n , which is consistent with the fact that Q_I and n are strongly positively correlated.

5.3 Implications for the Early Hadean Upper Mantle

Miyazaki & Korenaga (2022) assert that a hydrated and chemically heterogeneous mantle, a product of magma ocean solidification, may have been responsible for making the earth more habitable. It is a wet, pyroxenite-dominated mantle that would have accelerated the removal of atmospheric carbon dioxide, prompting the growth of oceans and the onset of plate tectonics. However, this study was limited to the investigation of dry samples of orthoenstatite, meaning that the flow-law parameters modeled are insufficient to make inferences about the rheology of the early Hadean upper mantle. Orthoenstatite is one of major phases in the modern mantle, next to olivine, in the form of peridotites and lherzolites. Despite that olivine is the most abundant mineral, orthoenstatite has been found to exert important effects on aggregate mechanical behavior (*Bystricky et al., 2016*). Though more data are required to accurately constrain the rheology of the early Hadean upper mantle, this analysis can still contribute to an improved understanding of the rheology of the modern mantle, thus current tectonic processes and mantle dynamics.

According to *Bystricky et al. (2016)*, orthoenstatite deforms about twice as slow as olivine under the same conditions, but as orthoenstatite has higher activation energy and a smaller stress exponent, the strength difference may decrease with increasing temperature and

decreasing stress, which are typical conditions in much of the upper mantle where these minerals are found.

However, olivine and enstatite have distinct rheological behaviors that depend on the conditions of deformation, as shown by orthoenstatite in this study. As this study does not address wet deformation, limiting our ability to extrapolate early Hadean mantle rheology, it also limits our ability to consider the mechanical behaviors of wet orthoenstatite and olivine, ignoring the impact water weakening may have on enstatite deformation and, in turn, mantle flow. In addition, upper mantle rheology cannot be fully realized without the parameterization of flow laws from lower-stress regimes, as the stresses studied in this paper are higher than those found in much of the upper mantle. This is exemplified by our weakly constrained diffusion creep parameters, reflecting our limited understanding of those deformation mechanisms in lower-stress regimes.

6. Conclusion

This study conducted a comprehensive reanalysis of the experimental data reported by *Bystricky et al.* (2016), which provided insights into the effectiveness of the MCMC inversion algorithm developed by *Korenaga and Karato* (2008) and *Mullet et al.* (2015) as well as the importance of composite rheology inversion with interrun biases. Further, we highlighted the significance of covariance analysis, from which the parameters derived by our MCMC inversions can be better understood.

However, to fully understand the rheological properties of the Hadean upper mantle, more data are needed, particularly for lower-stress conditions and wet deformation mechanisms. While illuminating, our analysis lacks proper constraints on the deformation mechanism for weak diffusion creep, highlighting the need for more experimental effort in this area. Ideally, experimental data would encompass regimes for diffusion creep mechanisms at varying levels of hydration, and analyzing such data through detailed statistical analysis would aid our ability to constrain the rheology of the mantle today and shortly after Earth's formation. Further, conducting better-controlled experiments under wet and high-pressure conditions would increase the quality of the data we use to constrain these properties, further advancing our understanding of mantle rheology.

Overall, a better understanding of the rheological properties of the Earth's mantle is imperative, as it plays a crucial role in the planet's tectonic processes and dynamics and may be the key to characterizing ambiguous processes fundamental to Earth's formation.

Acknowledgements

I would like to thank everyone who helped me construct and develop this senior essay. This includes my advisor, Professor Jun Korenaga, and my Dean of Undergraduate Studies, Professor Pincelli Hull, who have guided me throughout this project and the research process. I would also like to thank my professors in the Department of Earth and Planetary Sciences who have educated and inspired me, providing the foundations of my knowledge and ultimately shaping my passions for geology and the physical world.

References

- Bystricky, M., Lawlis, J., Mackwell, S., Heidelbach, F., and Raterron, P. (2016), High-temperature deformation of enstatite aggregates, *J. Geophys. Res. Solid Earth*, *121*, 6384–6400, doi:10.1002/2016JB013011.
- Dehghan, A., C. G. Sammis, and T. G. Langdon (1981), High temperature deformation of polycrystalline orthoenstatite under controlled oxygen fugacity, *Eos Trans. AGU*, *62*, 1029.
- Dehghan, A., T. G. Langdon, and C. G. Sammis (1982), High temperature creep of polycrystalline orthoenstatite, *Eos Trans. AGU*, *63*, 1094.
- Hitchings, R. S., M. S. Paterson, and J. Bitmead (1989), Effects of iron and magnetite additions in olivine-pyroxene rheology, *Phys. Earth Planet. Inter.*, *55*, 277–291.
- Ji, S. C., Z. Wang, and R. Wirth (2001), Bulk flow strength of forsterite-enstatite composites as a function of forsterite content, *Tectonophysics*, *341*, 69–93.
- Karato, S.-I.. *Deformation of Earth Materials: An Introduction to the Rheology of Solid Earth*. Cambridge University Press, 2008.
- Korenaga, J., and Karato, S.-I. (2008), A new analysis of experimental data on olivine rheology, *J. Geophys. Res.*, *113*, B02403, doi:10.1029/2007JB005100.
- Lawlis, J. D. (1998), High temperature creep of synthetic olivine-enstatite aggregates, PhD thesis, 133 pp., Pa. State Univ., University Park.

- Mackwell, S. J. (1991), High-temperature rheology of enstatite: Implications for creep in the mantle, *Geophys. Res. Lett.*, *18*, 2027–2030, doi:10.1029/91GL02492.
- Miyazaki, Y., and J. Korenaga. (2022), A wet heterogeneous mantle creates a habitable world in the Hadean. *Nature*, *603*, 86-90, doi:10.1038/s41586-021-04371-9.
- Mullet, B. G., Korenaga, J., and Karato, S.-I. (2015), Markov chain Monte Carlo inversion for the rheology of olivine single crystals. *J. Geophys. Res. Solid Earth*, *120*, 3142– 3172. doi: 10.1002/2014JB011845.
- Ohuchi, T., S. Karato, and K. Fujino (2011), Strength of single-crystal orthopyroxene under lithospheric conditions, *Contrib. Mineral. Petrol.*, *161*, 961–975, doi:10.1007/s00410-010-0574-3.
- Raleigh, C. B., S. H. Kirby, N. L. Carter, and H. G. Avé Lallemant (1971), Slip and clinoenstatite transformation as competing rate processes in enstatite, *J. Geophys. Res.*, *76*, 4011–4022, doi:10.1029/JB076i017p04011.
- Raterron, P., G. Frayse, J. Girard, and C. Holyoke III (2016), Strength of orthoenstatite single crystals at mantle pressure and temperature and comparison with olivine, *Earth Planet. Sci. Lett.*, *450*, 326–336, doi:10.1016/j.epsl.2016.06.025.
- Ross, J. V., and K. C. Nielsen (1978), High-temperature flow of wet polycrystalline enstatite, *Tectonophysics*, *44*, 233–261.
- Schloessin, H. H., and G. Ranalli (1988), Hot creep of single-crystals by bending: Procedure, theory and pilot experiment on enstatite, *Phys. Earth Planet. Inter.*, *52*, 132–149.

Appendix

Table 5. Creep Data for Enstatite Aggregates

Experiment	T (K)	dT	P_c (MPa)	dP_c	ϵ (s^{-1})	$d\epsilon$	σ (MPa)	$d\sigma$	d	dd
PI-512	1475	2	450	4	3.1×10^{-6}	4.0×10^{-7}	222	2	10	1
	1474				5.0×10^{-6}	6.0×10^{-7}	281			
	1473				8.0×10^{-6}	1.0×10^{-6}	336			
	1473				1.3×10^{-5}	2.0×10^{-6}	392			
	1473				1.1×10^{-5}	2.0×10^{-6}	367			
	1473				1.8×10^{-5}	5.0×10^{-6}	430			
	1473				7.7×10^{-6}	6.0×10^{-7}	312			
	1473				4.4×10^{-6}	5.0×10^{-7}	255			
	1473				3.2×10^{-6}	4.0×10^{-7}	226			
	1523				1.7×10^{-5}	2.0×10^{-6}	225			
	1523				2.7×10^{-5}	3.0×10^{-6}	283			
	1523				9.0×10^{-6}	1.1×10^{-6}	170			
	1523				1.2×10^{-5}	1.0×10^{-6}	199			
	1523				1.8×10^{-5}	2.0×10^{-6}	255			
	1523				4.0×10^{-5}	5.0×10^{-6}	342			
	1548				3.3×10^{-5}	4.0×10^{-6}	227			
	1473				1.2×10^{-5}	2.0×10^{-7}	406			
PI-539	1523	2	450	4	2.4×10^{-6}	5.0×10^{-7}	111	2	10	1
	1523				5.6×10^{-6}	8.0×10^{-7}	168			
	1523				1.1×10^{-5}	2.0×10^{-6}	224			
	1523				2.1×10^{-5}	4.0×10^{-6}	281			
	1523				3.4×10^{-5}	6.0×10^{-6}	334			
	1523				1.5×10^{-5}	2.0×10^{-6}	250			
	1523				8.0×10^{-6}	1.5×10^{-6}	195			

1523	3.9×10^{-6}	8.0×10^{-7}	138
1473	1.2×10^{-6}	2.0×10^{-7}	171
1473	2.3×10^{-6}	4.0×10^{-7}	228
1473	4.1×10^{-6}	8.0×10^{-7}	286
1473	7.3×10^{-6}	1.4×10^{-7}	344
1473	1.3×10^{-5}	2.0×10^{-6}	403
1473	2.3×10^{-5}	3.0×10^{-6}	460
1473	4.4×10^{-6}	7.0×10^{-7}	259
1501	6.8×10^{-6}	1.2×10^{-6}	230
1501	1.3×10^{-5}	1.0×10^{-6}	289
1501	3.6×10^{-5}	6.0×10^{-6}	407

Modified from *Bystricky et al.* (2016).